Indian J Phys (December 2022) 96(14):4091–4101
https://doi.org/10.1007/s12648-022-02360-w

ORIGINAL PAPER

Design parameters optimization of an electrothermal flow biosensor for the SARS-CoV-2 S protein immunoassay

S Kaziz[1,2]*, I Ben Mariem[1], F Echouchene[3], M H Gazzah[1] and H Belmabrouk[3,4]

[1]Quantum and Statistical Physics Laboratory, Faculty of Sciences of Monastir, University of Monastir, Environment Boulevard, 5019 Monastir, Tunisia

[2]Higher National Engineering School of Tunis, Taha Hussein Montfleury Boulevard, University of Tunis, 1008 Tunis, Tunisia

[3]Laboratory of Electronics and Microelectronics, Faculty of Science of Monastir, University of Monastir, Environment Boulevard, 5019 Monastir, Tunisia

[4]Department of Physics, College of Science at Al Zulfi, Majmaah University, Al Majma'ah 11952, Saudi Arabia

Received: 03 January 2022 / Accepted: 25 March 2022 / Published online: 18 April 2022

Abstract: To combat the coronavirus disease 2019 (COVID-19), great efforts have been made by scientists around the world to improve the performance of detection devices so that they can efficiently and quickly detect the virus responsible for this disease. In this context we performed 2D finite element simulation on the kinetics of SARS-CoV-2 S protein binding reaction of a biosensor using the alternating current electrothermal (ACET) effect. The ACET flow can produce vortex patterns, thereby improving the transportation of the target analyte to the binding surface and thus enhancing the performance of the biosensor. Optimization of some design parameters concerning the microchannel height and the reaction surface, such as its length as well as its position on the top wall of the microchannel, in order to improve the biosensor efficiency, was studied. The results revealed that the detection time can be improved by 55% with an applied voltage of 10 V_{rms} and an operating frequency of 150 kHz and that the decrease in the height of the microchannel and in the length of the binding surface can lead to an increase in the rate of the binding reaction and therefore decrease the biosensor response time. Also, moving the sensitive surface from an optimal position, located in front of the electrodes, decreases the performance of the device.

Keywords: Biosensor; SARS-CoV-2 S protein; ACET flow; Design parameters; Detection time

1. Introduction

Officially more than 5 million deaths from COVID-19 have been recorded since the appearance of this disease at the end of December 2019 in Wuhan in China [1]. This increase in the death rate has led scientists all over the world to conduct a great deal of research to tackle the rapid spread of SARS-CoV-2 which is the virus responsible for this disease [2]. Although the development of an effective vaccine for all variants may take months or even years, the early detection of infected patients seems to be one of the best ideas for controlling the situation. It is for this reason that the applications of new detection techniques with high affinity, specificity and sensitivity are becoming more and more important. Among these detection techniques, microfluidic biosensors have played an essential role in the fight against this pandemic in the latest investigations [3–5]. Nonetheless, the dependence of their efficiency on the binding reaction which is generally restricted by the low diffusion rate of the target analytes and therefore a long detection time limits their use in different situations [6, 7]. The binding reaction between the analytes and the ligands immobilized on the sensitive surface leads to the formation of analyte-ligand complexes on this surface, the concentration of which has a determining role for the detection process.

Regarding SARS-CoV-2 each virus has four structural proteins named the spike glycoprotein S, the envelope protein E, the membrane protein M and the nucleocapsid protein N, and other accessory proteins. S protein is the most widely used antigenic biomarker for the detection of

*Corresponding author, E-mail: kaziz_sameh@yahoo.fr

COVID-19 because it can attach very easily to the cell receptor called angiotensin converting enzyme 2, ACE2, located on the surface of human cells [8]. The high affinity between the S protein and ACE2 increases the infectivity of SARS-CoV-2.

Currently most laboratories use a molecular method called quantitative real-time polymerase chain reaction (qRT-PCR) [9] for the detection of viruses in respiratory infections. This method is well established, it can detect even tiny amounts of viruses [10] but it requires well-equipped laboratories, it can also take time and above all it can be prone to errors [11, 12]. Serological tests such as enzyme-linked immunosorbent assays (ELISA), lateral flow immunoassays (LFIA) and chemiluminescent immunoassays (CLIA), can also be used to determine the presence of antibody caused by SARS-CoV-2 virus [13]. However, these tests are further efficient in the subsequent phases [14] and cannot be used for early diagnosis. Point-of-care (POC) biosensors that are also used for rapid diagnosis of COVID-19 disease are polydimethylsiloxane (PDMS) chip-based biosensors or paper-based biosensors, such as lateral flow test strips [10, 15]. These tests are widely used to detect antibodies, antigens, or nucleic acids in raw samples (saliva, sputum, and blood) [16]. Compared to existing POC biosensors, qRT-PCR shows higher clinical sensitivity and specificity.

Many physical mechanisms have been used to improve the biosensor binding reaction rate, such as hydrodynamic pressure [17], AC electrokinetics (ACEK) [18–21], magnetic effect [22] and optical forces [23]. For the ACET effect, it is necessary to be vigilant on the applied voltage in order to create the electrothermal force because beyond a limit value, the increase in the temperature within the microchannel exceeds the authorized thresholds and can thus damage the nature of the biofluids [24, 25]. Other studies have shown that several manufacturing parameters can be adjusted to improve the performance of a biosensor [7, 26]. Shahbazi et al. [27] studied the impact of certain conception parameters on the saturation time of biosensors intended for the recognition of coronaviruses. The study revealed that moving the reaction surface position by just 500 µm decreased the saturation time by further than 50%.

To help in solving the problem of the target analyte diffusion boundary layer usually formed in the vicinity of the sensitive surface, we developed a two-dimensional simulation using the finite element method to first show the impact of the electrothermal force on the kinetics of the SARS-CoV-2 S protein binding reaction, and then to examine the effects of changing the height of the microchannel and the length and position of the reaction surface on the biosensor efficiency.

2. Theoretical modeling

2.1. Geometrical configuration

As shown in Fig. 1, the microfluidic biosensor studied measures 250 µm in length (L) and 40 µm in width (H). The reaction surface, of length (l_S) of 20 µm is placed on the upper wall of the microchannel and two electrodes, each having a length (l_E) of 60 µm, are located on the bottom wall of the microchannel. The gap between the two electrodes is fixed at 20 µm.

2.2. Electric modeling

The following Poisson equation is used to calculate the electric field $\vec{E}$ expressed by the negative gradient of electrical potential V which is created by the external potential applied through the electrodes.

$$\Delta V = 0;\ \vec{E} = -\nabla V \tag{1}$$

2.3. Temperature modeling

The following thermal energy equation is used to calculate the temperature field T:

$$\rho C_p \vec{\boldsymbol{u}} \cdot \nabla T = \lambda \Delta T + \sigma \left|\vec{\boldsymbol{E}}\right|^2 \tag{2}$$

where ρ, λ, C_p and σ are, respectively, the density, the thermal conductivity, the specific heat at constant pressure, and the electrical conductivity of the carrier fluid. The term source, $\sigma\left|\vec{E}\right|^2$, represents the Joule heating term [28]. Thermal conductivity λ and specific heat at constant pressure C_p are assumed to be independent of the fluid temperature rise, which is generally low [29, 30].

2.4. Flow velocity modeling

The next Navier–Stokes equations expressed for an incompressible, homogeneous, and Newtonian fluid in laminar flow are used to calculate the pressure and velocity fields:

$$\nabla.\vec{\boldsymbol{u}} = 0 \tag{3}$$

$$\rho(\vec{\boldsymbol{u}}.\nabla)\vec{\boldsymbol{u}} = -\nabla p + \mu\nabla^2\vec{\boldsymbol{u}} + \overrightarrow{\boldsymbol{F_e}} \tag{4}$$

where $\overrightarrow{F_e}$ defines the electrothermal force, p is the pressure and μi s the dynamic viscosity of the carrier fluid. The inlet velocity is parabolic having the following form:

$$\boldsymbol{u}(0,y) = 4\boldsymbol{u}_{\max}\frac{y}{H}\left(1-\frac{y}{H}\right) \tag{5}$$

where $u_{\max}$ is the maximum velocity at the center of the

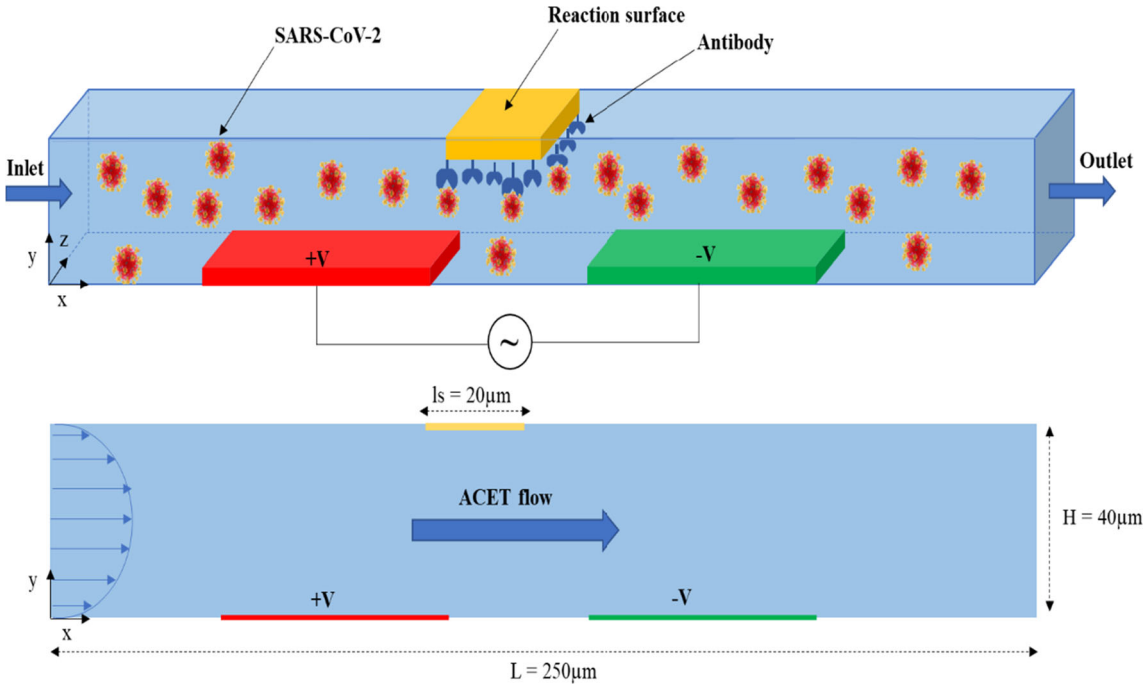

Fig. 1 Geometric configuration of the microfluidic biosensor

microchannel. When an alternating voltage is applied, the nonuniform Joule heating engenders a temperature gradient in the fluid giving rise to gradients of electrical permittivity and conductivity which are responsible for the desired electrothermal force. The time average value of this force is defined by:

$$\vec{F}_e = -\frac{1}{2}\left(\frac{\nabla\sigma}{\sigma} - \frac{\nabla\varepsilon}{\varepsilon}\right)\cdot\vec{E}\frac{\varepsilon\vec{E}}{1+(\omega\tau)^2} - \frac{1}{4}\nabla\varepsilon\left|\vec{E}\right|^2 \tag{6}$$

here ε is the permittivity, $\omega = 2\pi v$ is the angular frequency of the AC voltage signal and $\tau = \varepsilon/\sigma$ is the fluid charge relaxation time.

Conforming to Green et al. [29], we get:

$$\frac{1}{\varepsilon}\frac{\partial\varepsilon}{\partial T} = -0.004 \Rightarrow \frac{\nabla\varepsilon}{\varepsilon} = \frac{1}{\varepsilon}\frac{\partial\varepsilon}{\partial T}\nabla T = -0.004\nabla T \tag{7}$$

$$\frac{1}{\sigma}\frac{\partial\sigma}{\partial T} = 0.02 \Rightarrow \frac{\nabla\sigma}{\sigma} = \frac{1}{\sigma}\frac{\partial\sigma}{\partial T}\nabla T = 0.02\nabla T \tag{8}$$

So, the expression of the electrothermal force becomes:

$$\vec{F}_e = -0.012\left(\nabla T\cdot\vec{E}\right)\frac{\varepsilon\vec{E}}{1+(\omega\tau)^2} + 0.001\left(\varepsilon\left|\vec{E}\right|^2\right)\nabla\mathrm{T} \tag{9}$$

2.5. Surface and analyte concentrations modeling

The transport of SARS-CoV-2 viruses by diffusion and convection is modeled by the following equation:

$$\frac{\partial[A]}{\partial t} + \vec{u}\cdot\nabla[A] = D\Delta[A] \tag{10}$$

where $[A]$ is the concentration of the aimed analyte (SARS-CoV-2) and D is its diffusion constant. To solve the

Table 1 Boundary conditions

Type	(V)	(T)	(u)	$([A])$
Microchannel walls	$\frac{\partial[V]}{\partial n} = 0$	$\frac{\partial[T]}{\partial n} = 0$	$u = 0$	$\frac{\partial[A]}{\partial n} = 0$
Binding surface	$\frac{\partial[V]}{\partial n} = 0$	$\frac{\partial[T]}{\partial n} = 0$	$u = 0$	$\frac{\partial[A]}{\partial n} = -\frac{1}{D}\frac{\partial[AB]}{\partial t}$
Electrodes	$\pm V_{\mathrm{rms}}$	T_0	$u = 0$	$\frac{\partial[A]}{\partial n} = 0$
Microchannel inlet	$\frac{\partial[V]}{\partial n} = 0$	$\vec{n}.(\lambda\nabla T) = 0$	u (0, y)	$[A]_0$
Microchannel outlet	$\frac{\partial[V]}{\partial n} = 0$	$\vec{n}.(\lambda\nabla T) = 0$	$\frac{\partial[u]}{\partial n} = 0$	$\vec{n}.(D\nabla[A]) = 0$

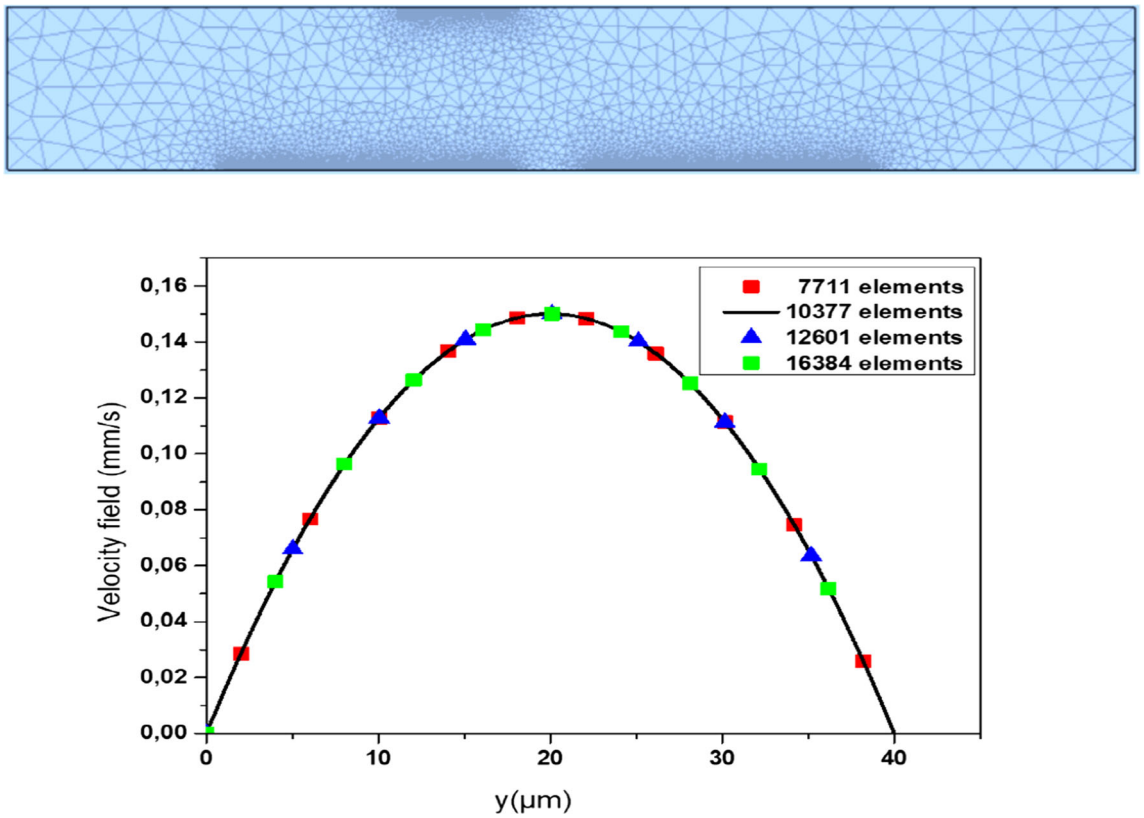

Fig. 2 (a) Representation of the 2D domain meshing, (b) Velocity field at x = 100 μm of the microchannel for several mesh grids

Fig. 3 The normalized complex concentration, $\boxed{AB}$, over time. Validation of the current mathematical model compared to the experimental study of Berthier and Silberzan [35]

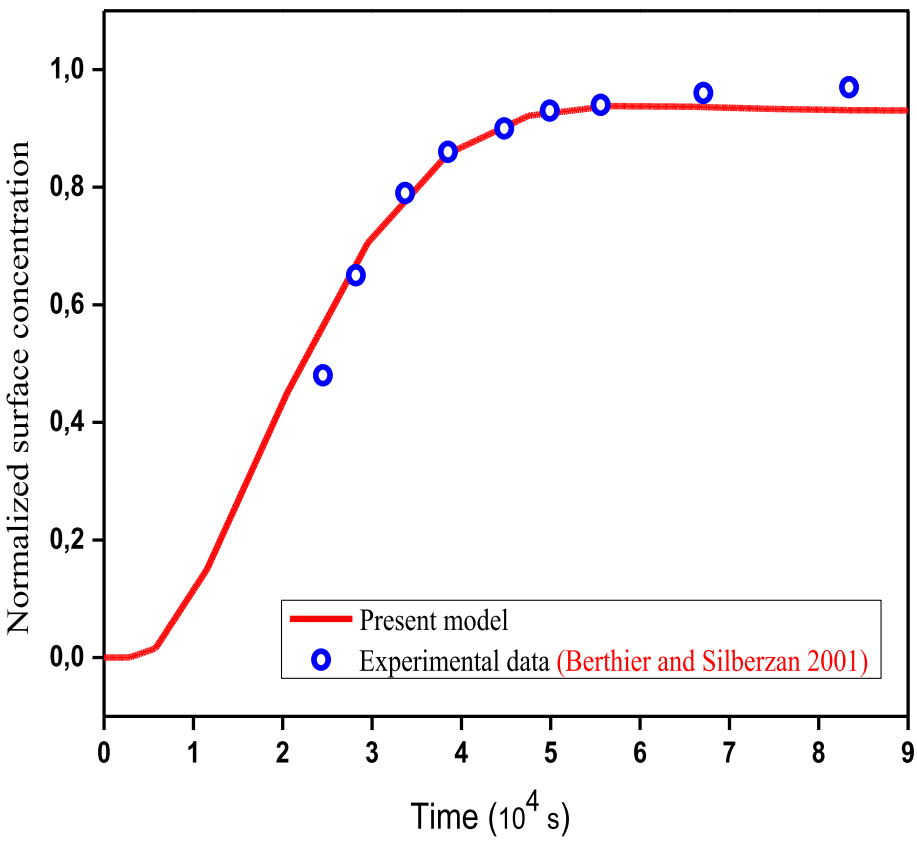

Table 2 Model parameters

Constant	Name	Value
K_{on}	Association constant	10^3 (m^3/Mol s)
K_{off}	Dissociation constant	10^{-3} (s^{-1})
D	Diffusion constant	10^{-11} (m^2/s)
$[B_{max}]$	Ligand concentration	33.10^{-8} (Mol/m^2)
$[A]_0$	Analyte input concentration	1.10^{-9} (Mol/m^3)
λ	Thermal conductivity	0.6 [W/(K m)]
ρ	Fluid density	1000 (kg/m^2)
μ	Dynamic viscosity	1.08×10^{-3} (Pa s)
Cp	Specific heat	4.184 [kJ/(kg K)]
σ	Electrical conductivity	5.75×10^{-2} (S/m)
ε_r	Relative permittivity	80.2
ν	Frequency	100 (kHz)

chemical kinetics equation, the first-order Langmuir–Hinshelwood adsorption model [31, 32] is employed.

$$\frac{\partial[AB]}{\partial t} = k_{on}[A_{surf}]\{[B_{max}] - [AB]\} - k_{off}[AB] \quad (11)$$

where k_{on} and k_{off} are the association and dissociation constants, respectively, $[A_{surf}]$ is the concentration of aimed analyte at the reaction surface, $[AB]$ is the complex concentration at the binding surface and $[B_{max}]$ is the immobilized antibody concentration on the reaction surface [33].

3. Boundary and initial conditions

To obtain the electric potential distribution, electric potential levels of $\pm V_{rms}$ are applied to the electrodes and the other walls of the microchannel are electrically insulated. To achieve the distribution of the temperature field, the electrodes are set to ambient temperature T_0, due to the high thermal conductivities of common electrode materials, also a heat flow is applied to the inlet and outlet of the microchannel and the remaining surfaces are assumed to be adiabatic. For the fluid flow, the non-slip conditions are applied to the side surfaces of the microfluidic device, a parabolic velocity profile is given to the carrier fluid at the inlet of the microchannel and at the outlet, the flow was assumed to be fully developed, then the gradient of the axial velocity in the axial direction was set to zero. For analyte transport and binding reaction, a low concentration of analyte is injected at the inlet and the convective flow condition is applied at the outlet. On the sensitive surface, the diffusive flux condition generated by the binding reaction between analytes and ligands is applied and the homogeneous Neumann condition is used for the other walls and the electrodes because they are assumed to be impermeable and do not interact with the target analyte [27]. All the boundary conditions for electric potential, temperature, velocity, and analyte concentration used in this model are summarized in Table 1 where $\vec{n}$ is the unit normal vector to the surface.

The initial velocity of the fluid within the microchannel was assumed to be zero. The concentration of analyte

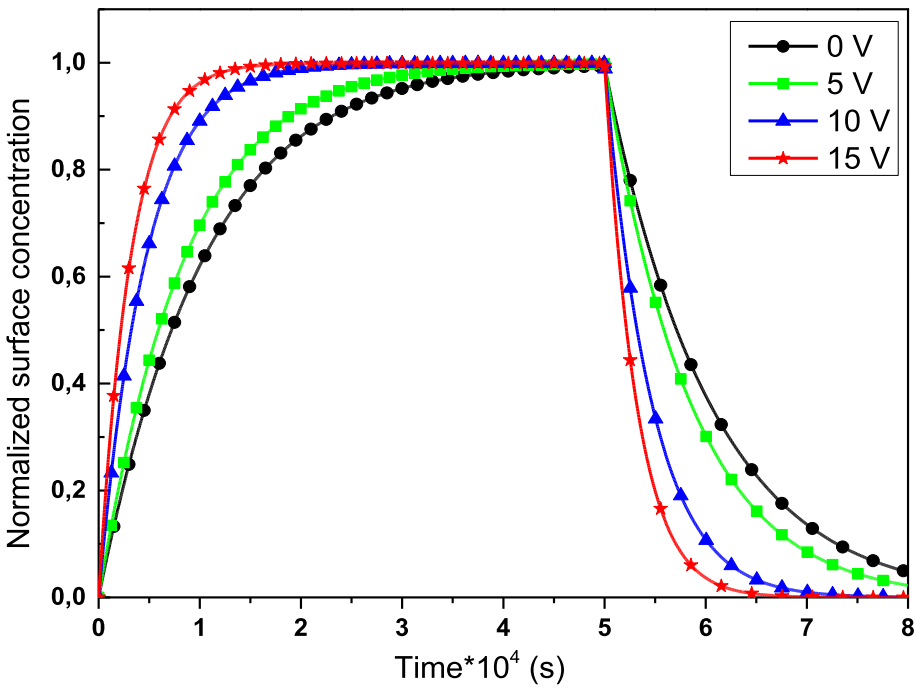

Fig. 4 Effect of various applied voltages. Temporal progression of the surface concentration normalized at binding sites, $[\overline{AB}]$, with or without electric excitation

Table 3 Detection time, temperature growth and drop percentage for various applied voltages

Used voltage (V)	Detection time (s)	Temperature growth (K)	Drop percentage (%)
0	29,650	–	–
5	24,200	1.2	18
10	13,375	4.8	55
15	9150	10.8	69

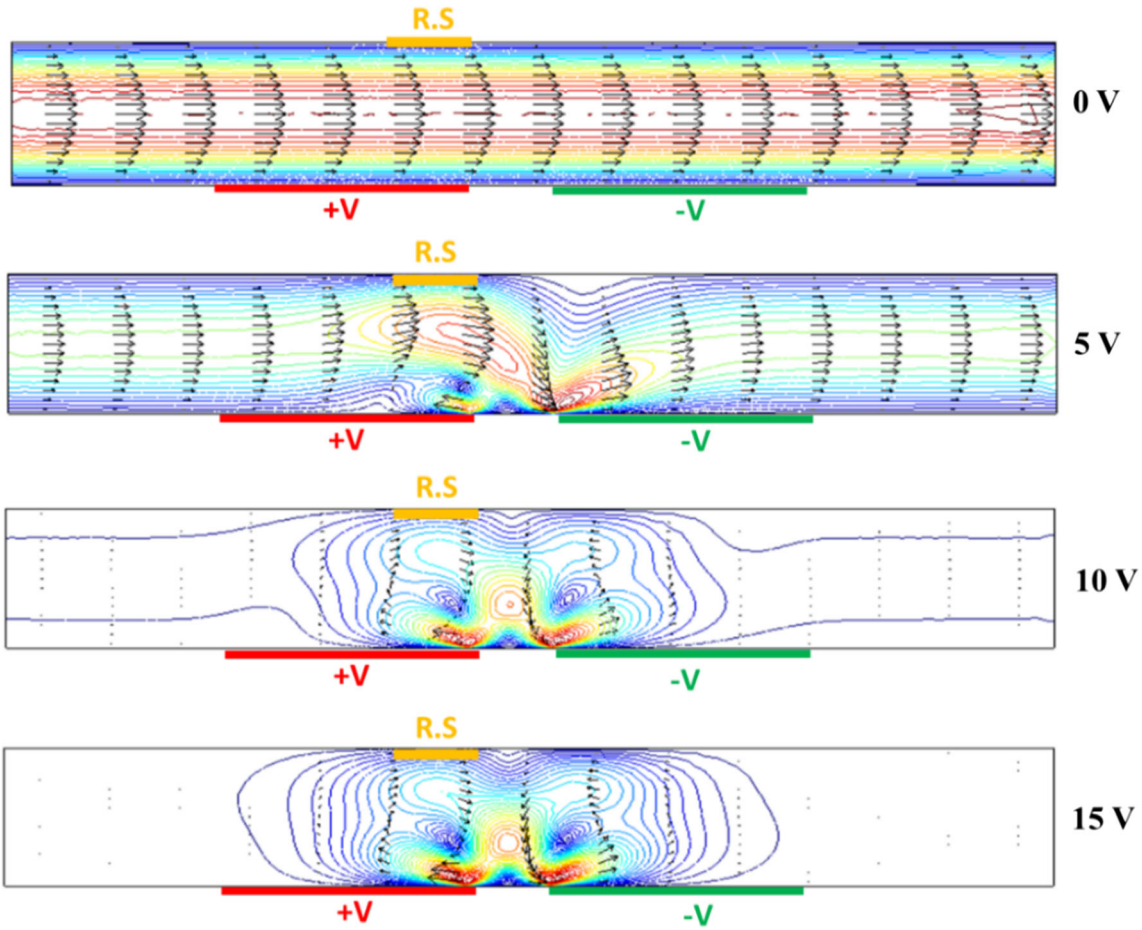

Fig. 5 Flow lines and velocity field without and with the ACET effect

$[A]_{(t=0)}$, and the surface analyte/ligand concentration, $[AB]_{(t=0)}$, were initially zero.

4. Numerical method

The proposed model equations were solved using Galerkin finite element analysis [34]. We used 10,377 triangular geometric elements for the whole 2D domain including the refined elements of the reaction surface and the electrodes, as presented in Fig. 2a. To confirm that convergence has been reached and that the calculated results are independent of the mesh size, Fig. 2b shows the velocity field at x = 100 μm of the microchannel for several mesh grids, namely 7711, 10,377, 12,601 and 16,384 elements, without electrothermal effect. The obtained variations using different element numbers are significantly similar. First, the electric field within the fluid was calculated using Eq. (1), then the temperature, pressure, and velocity fields were calculated by simultaneously solving Eqs. (2–4) in stationary mode and finally, the concentrations of analytes and the analyte-ligand complexes, formed on the binding

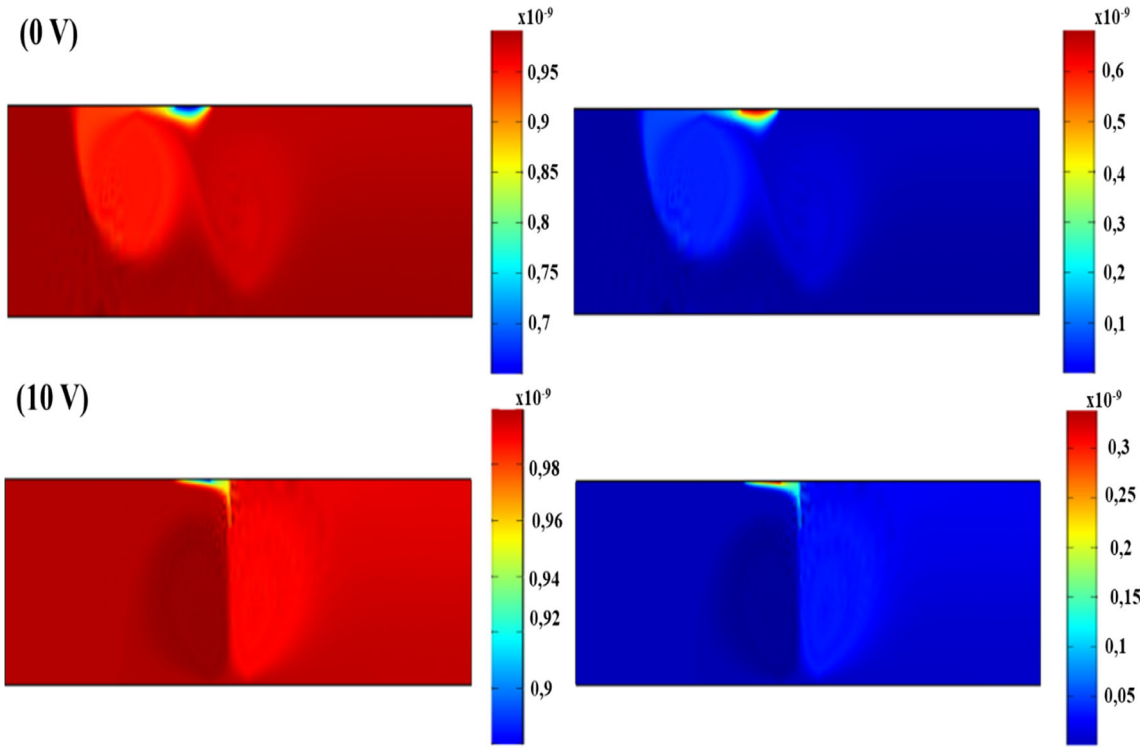

Fig. 6 Diffusion boundary layers in association (left panel) and dissociation (right panel) phases without and with electrothermal effect

surface, as a function of time were simulated from the coupled Eqs. (10) and (11). The complex concentration at the binding surface $[AB]$ is obtained by integrating its spatial value over the reaction surface length using the following equation:

$$[AB](t) = \frac{1}{l_s}\int_0^{l_s}[AB](x,t)\mathrm{d}x \tag{12}$$

5. Results and discussion

5.1. Model validation

First, the validity of the model was checked by the experimental data of Berthier and Silberzan [35], without electrothermal effect. Figure 3 demonstrates the normalized concentration of analyte-ligand complexes formed at the sensitive surface during the adsorption phase as a function of time for a microfluidic channel biosensor of dimensions of 10mmx1mm. The concentration of analytes is 2.5×10^{-6} Mol/m^3 and that of ligands is 1.668×10^{-8} Mol/m^2. The association and dissociation constants are, respectively, 75 m^3/Mol s and 10^{-2} 1/s and the diffusion coefficient is 7×10^{-11} m^2/s. A great accord between experimental data points and our numerical results was recorded.

5.2. ACET impact on the kinetics of the binding reaction

In this section, we studied the impact of the ACET flow on the binding kinetics of the SARS-CoV-2 S protein. The used Physicochemical parameters [36] are presented in Table 2.

The normalized surface concentration over time has been plotted in Fig. 4. As illustrated, a progress in the binding reaction is noted by applying an electric field. The response time, the drop percentage, and the temperature growth for the several applied voltages are given in Table 3. Detection time corresponds to the time necessary for having 95% of the response. We can see that the detection time decreases with the increase in the applied voltage. However, the voltage 10 V can be considered as an optimal voltage for the electrothermal effect because the heating of the fluid generated by this voltage reaches the limit ($\Delta T < 5$ K) which leaves the electrical and thermal properties of the fluid unchanged as assumed in such a model.

Figure 5 shows the current lines and the velocity fields for 0, 5, 10 and 15 V applied voltages. As expected, the electrothermal effect generates asymmetric eddy patterns in the fluid close to the electrodes. The size and the number of these vortexes increase with the increase in the applied voltage. Therefore, it can be concluded that the ACET flux

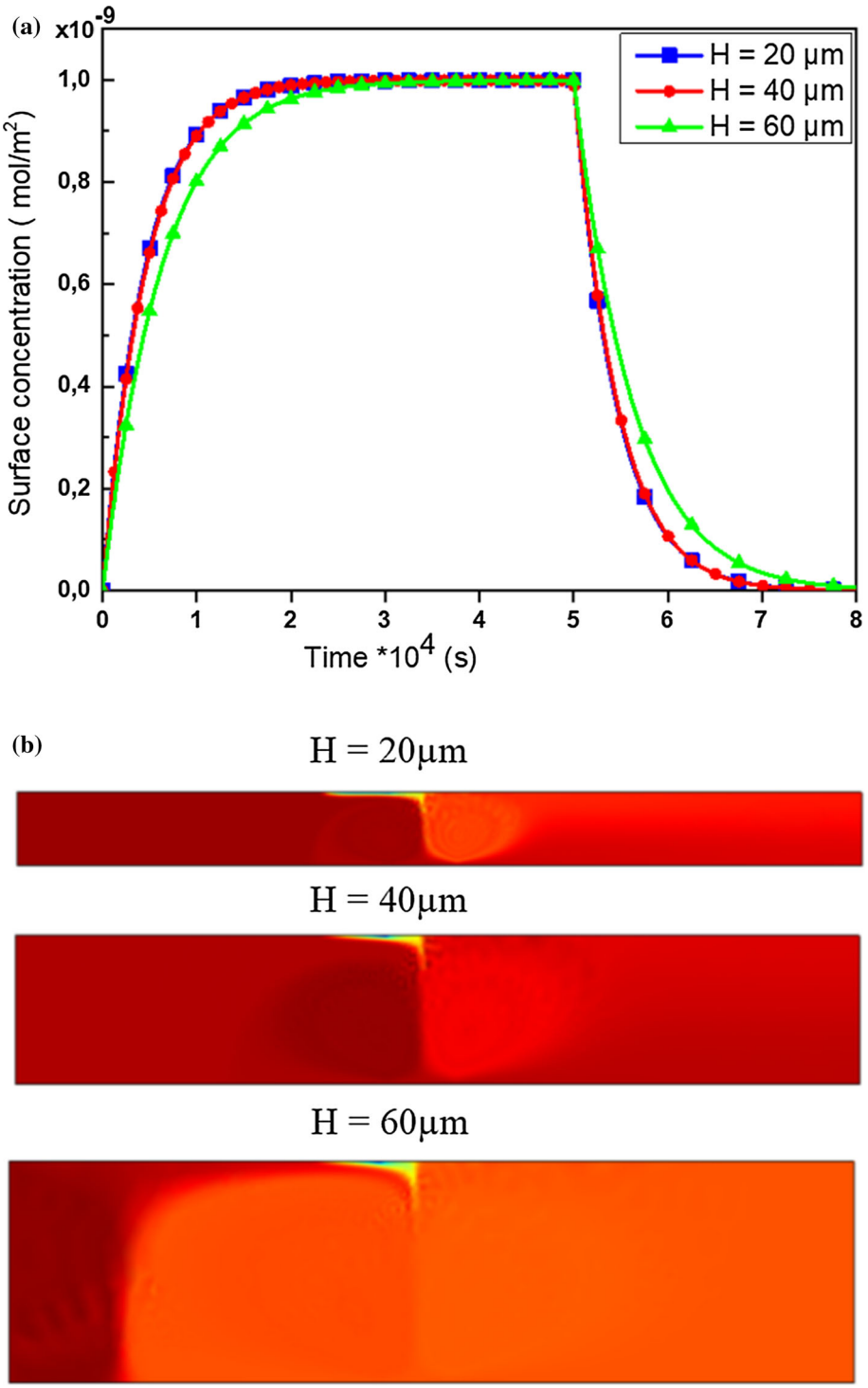

Fig. 7 Microchannel height effects. (**a**): Surface concentration of SARS-CoV-2–antibody complexes with different microchannel heights. (**b**): Diffusion boundary layers of analyte concentration in association phases for different microchannel heights

generated vortices, thereby stirring the flux, which boosts the mass transport of analyte and decreases the diffusion boundary layer thickness.

Figure 6 shows the analyte concentration diffusion boundary layers in both, association and dissociation, phases without and with electrothermal effect. It can be noted that, in the two phases, the diffusion boundary layers with an applied optimal voltage of 10 V are much thinner than those obtained without an applied voltage (0 V). It can then be concluded that under the electrothermal effect, the concentration of analytes is more condensed near the sensitive surface, during the adsorption phase, and less present during the desorption phase, which accelerates the kinetics

of the binding reaction and consequently reduces the detection time of the device.

5.3. Microchannel height effect on binding reaction kinetics

Logically the thinnest microchannel should have a better binding reaction kinetics than the larger one because for the thinnest microchannel the quantity of analyte is denser. Figure 7a shows a comparison of the binding kinetics of SARS-CoV-2 S protein in three microchannels of various heights of 20, 40 and 60 µm, respectively, at the same fluid velocity, u_{max} = 15.10^{-4} m/s, and the same applied voltage, 10 V. We found that the binding reactions and thus the detection times in the 20 and 40 µm high microchannels are almost the same and are enhanced compared to those obtained with a 60 µm high microchannel (Table 4).

Figure 7b shows that the diffusion boundary layers of the analyte concentration just in the vicinity of the reaction surface at the adsorption times are almost identical and relatively thin but with more pronounced analyte condensation in the two thinnest microchannels, which means that mass transport is sufficient for analyte-ligand binding for the three-different microchannels but more accelerate for the thinner ones. Therefore, for heterogeneous immunoassays, narrow microchannels are preferred if there is no fabrication or blocking problems because they consume less analyte quantity at the same fluid flow rate.

Table 4 Detection time for different microchannel height

Microchannel height (µm)	Detection time (s)
20	13,325
40	13,375
60	18,150

5.4. Reaction surface length effect on binding reaction kinetics

We further illustrate the ability to apply electrothermal force to restrain the development of the boundary layer diffusion and improve biosensor efficiency by analyzing SARS-CoV-2 binding reaction curves with different reaction surface lengths, while maintaining the same

Table 5 Detection time for different reaction surface lengths

Reaction surface length (µm)	Detection time (s)
20	13,375
40	16,475
60	18,025
80	22,550

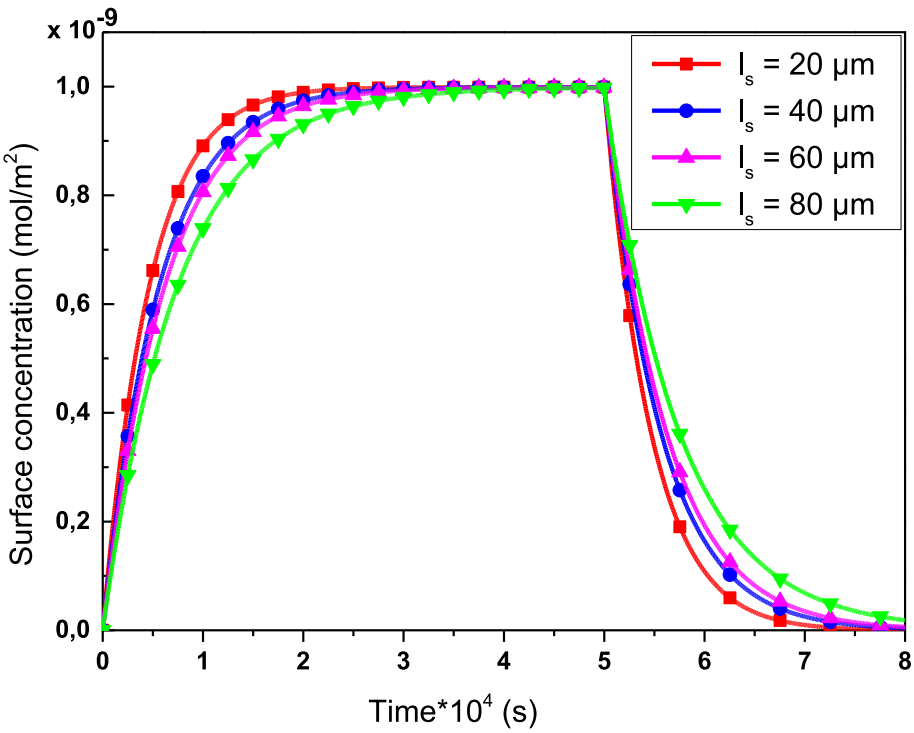

Fig. 8 Surface concentration over time with various reaction surface lengths

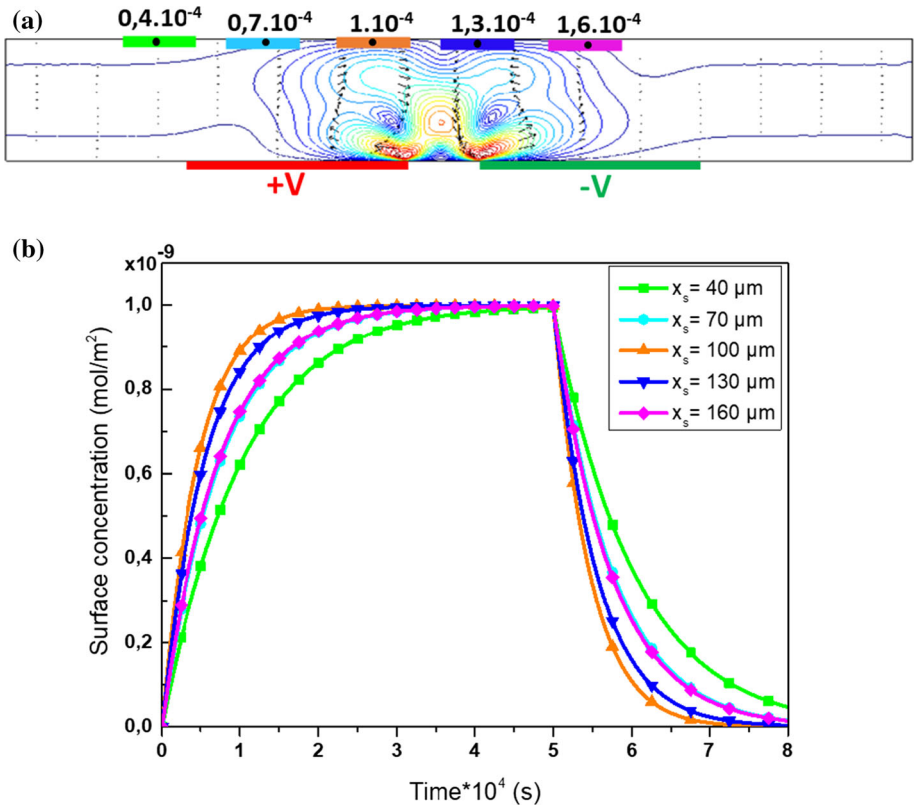

Fig. 9 Effects of reaction surface position on binding kinetics. (**a**) Five different positions of the reaction surface. (**b**) Temporal evolution of the surface concentration with various reaction surface positions

Table 6 Detection time for various reaction surface positions

Reaction surface position X_s (µm)	Detection time (s)
40	29,625
70	22,000
100	13,375
130	16,200
160	21,625

concentration of ligands initially immobilized to this surface. Figure 8 shows the sketch of four different lengths, namely 20, 40, 60 and 80 µm. The simulation results clearly indicate that the shorter the reaction surface, the shorter the response time (Table 5) and the faster the binding reaction is.

5.5. Reaction surface position effect on binding reaction kinetics

For a well analysis of the evolution of the performance of the biosensor, the detection time as a function of the position of the functionalized surface with respect to the inlet plane was also investigated. Five positions were analyzed as illustrated in Fig. 9a, with 10 V electrothermal effect. The central location of the biosensor (x_s) for the first case is positioned 40 µm from the inlet plane. The following cases are moved at 30 µm intervals toward the outlet. As shown in Fig. 9b and Table 6, when the biosensor is moved away from the inlet, its detection time decreases until it has a better value at 100 µm position, then it increases again as the biosensor moves away from this optimal position toward the outlet of the microchannel. Although movements occur at the same rate, before and after the optimal position, detection times do not vary at the same rate.

6. Conclusions

For sensitive and reliable detection of COVID-19 disease, we performed a 2D simulation of microfluidic biosensor for the binding kinetics of SARS-CoV-2 S protein using the electrothermal effect. The results showed that the electrothermal force improved the binding efficiency of biosensor and the enhancement was about 55% with an optimum applied voltage of 10 V. Some design parameters were analyzed in order to optimize the performance of the microfluidic biosensor. Three different heights of the microchannel and five cases of reaction surface positions on the top wall of the microchannel are studied to indicate their influences on the efficiency of the binding reaction. We have also showed that the decrease in the length of the

binding surface can lead to an increase in the rate of the binding reaction.

Declarations

Conflict of interest The authors announce that they have no known competing financial interests or personal relationships that could have appeared to influence the work reported in this paper.

References

[1] T Riffe and E Acosta *Int. J. Epidemiolo.* **50** 390 (2021)
[2] N Ben-Khedher, L Kolsi and H Alsaif *Alex. Eng. J.* **60** 3965 (2021)
[3] H B Lee, M Meeseepong, T Q Trung, B Y Kim and N E Lee *Biosens. Bioelectron.* **156** 112133 (2020)
[4] E Morales-Narvaez and C Dincer *Biosens. Bioelectron.* **163** 112274 (2020)
[5] H Zhu, Z Fohlerova, J Pekarek, E Basova and P Neuzil *Biosens. Bioelectron.* **153** 112041 (2020)
[6] H Nygren, M Werthen and M Stenberg *J. Immunol. Methods.* **101** 63 (1987)
[7] C K Yang, J S Chang, S D Chao and K C Wu *J. Appl. Phys.* **103** 084702 (2008)
[8] Y Huang, C Yang, Xu Xf, W Xu and S W Liu *Acta Pharmacol. Sin.* **41** 1141 (2020)
[9] V M Corman et al *Euro Surveill.* **25** 2000045 (2020)
[10] J R Choi *Front. Chem.* **8** 517 (2020)
[11] S V Vemula, J Zhao, J Liu, X Wang, S Biswas and I Hewlett *Viruses.* **8** 96 (2016)
[12] C T Pachucki, M A Khurshid and J Nawrocki *Clin. Microbiol.* **42** 2796 (2004)
[13] K L Chew et al. *Clin. Microbiol. Infect.* **26** 1256.E9 (2020)
[14] A Ghaffari, R Meurant and A Ardakani *Diagnostics* **10** 453 (2020)
[15] C Sheridan *Nat. Biotechnol.* **38** 515 (2020)
[16] J Zhifeng, A Feng and T Li *J. Clin. Virol.* **127** 104359 (2020)
[17] Y J Chiu, S H Cho, Z Mei, V Lien, T F Wu and Y H Lo *Lab Chip* **1** 1803 (2013)
[18] K Yang, N Islam, S Eda and J Wu *Microfluid. Nanofluid.* **21** 35 (2017)
[19] S Kaziz, Y Saad, M Bouzid, M Selmi and H Belmabrouk *Microfluid. Nanofluid.* **25** 86 (2021)
[20] M Selmi, M H Gazzah and H Belmabrouk *Langmuir* **32** 13305 (2016)
[21] H Hajji, L Kolsi, K Ghachem, C Maatki and M N Borjini *Alex. Eng. J.* **59** 1649 (2020)
[22] Y Saad, M Selmi, M H Gazzah and H Belmabrouk *Eur. Phys. J. Plus.* **136** 608 (2021)
[23] G U Lee, S Metzger, M Natesan, C Yanavich and Y F Dufrêne *Anal. Biochem.* **287** 261 (2000)
[24] M Lian, N Islam and J Wu *IET Nanobiotechnol.* **1** 36 (2007)
[25] S Kaziz, Y Saad, M H Gazzah and H Belmabrouk *Eur. Phys. J. Plus.* **137** 241 (2022)
[26] H Hajji, L Kolsi, W Hassen, A A A Al-Rashed, M N Borjini and M A Aichouni *Phys. E Low-Dim. Syst. Nanostruct.* **104** 177 (2018). https://doi.org/10.1016/j.physe.2018.07.034
[27] F Shahbazi, M Jabbari, M N Esfahani and A Keshmiri *Biosensors Bioelectron.* **171** 112716 (2021)
[28] G Soni, M Singurdson and C Meinhart *Model Library, MEMS Module COMSOL Multiphysics.* **V3.5a** 220 (2008)
[29] N G Green, A Ramos, A González and A Castellanos *Electrothermal. J. Electrostat.* **53** 71 (2001)
[30] A Ramos, H Morgan, N G Green and A Castellanos *J Phys. D Appl. Phys.* **31** 2338 (1998). https://doi.org/10.1088/0022-3727/31/18/021
[31] M Selmi, M H Gazzah and H Belmabrouk *Sci Rep.* **7** 1 (2017)
[32] M Selmi, F Echouchene, M H Gazzah and H Belmabrouk *IEEE Sensors J.* **15** 7321 (2015)
[33] M Selmi and H Belmabrouk *Micromachines.* **11** 342 (2020)
[34] Z Chen *Finite Element Methods, and Their Applications (Scientific Computation)* (Berlin: Springer) (2005)
[35] J Berthier and P Silberzan *Microfluidics for Biotechnology* (Artech House) (2010)
[36] C Qi, J Z Duan, Z H Wang, Y Y Chen, P H Zhang, L Zhan, X Y Yan and W C Cao *Biomed. Microdevices.* **8** 247 (2006)